Materials Science & Engineering A 814 (2021) 141219

Contents lists available at ScienceDirect

Materials Science & Engineering A

journal homepage: http://www.elsevier.com/locate/msea

Analysis of the elevated temperature deformation mechanisms and grain boundary strengthening of the alumina-forming austenitic stainless steel Fe–20Cr–30Ni–2Nb–5Al

Andrew Peterson *, Ian Baker

Thayer School of Engineering, Dartmouth College, Hanover, NH, 03755, USA

ARTICLE INFO

Keywords:
AFA steel
Deformation
Creep
Precipitates
Grain boundary

ABSTRACT

The deformation mechanisms of an alumina-forming austenitic stainless-steel Fe–20Cr–30Ni–2Nb–5Al (at. %) were investigated at 750 °C using both creep tests and strain rate jump tests. It was found that nano-sized $L1_2$-structured precipitates were the dominant precipitate in the matrix and provided the majority of the strengthening. This behavior could be modeled well using a threshold stress term in a power law creep equation. Additionally, there appears to be a grain boundary strengthening mechanism in which the grain boundaries covered by precipitates act as barriers to dislocation movement. This could be again modeled using a power law creep equation. In addition to blocking dislocations, the grain boundary precipitates also prevent grain boundary sliding during creep. While the grain boundaries showed several strengthening mechanisms, all tests ultimately failed along the grain boundaries.

1. Introduction

Alumina-forming austenitic stainless steels (AFAs) show promise as a class of materials suitable for high temperature applications, especially for power generation. Higher system efficiency can be attained at higher temperatures, which in turn leads to a reduction in harmful emissions [1,2]. Operating at these temperatures requires a material that is strong, displays good oxidation and corrosion resistance, and is economically viable [1]. Nickel-based superalloys satisfy the materials property requirements, however, they are prohibitively expensive [3]. AFAs have the potential to meet all of the above requirements [4–7]. AFAs use alumina as a protective oxide scale, which has previously been demonstrated to provide very good oxidation resistance at high temperature [8,9]. AFAs are further strengthened with Laves phase precipitates in the matrix and on the grain boundaries (GBs) [3,7,10,11]. In the newer families of AFAs, nano-sized MC carbides or $L1_2$-structured Ni_3Al precipitates are also used as strengtheners in the matrix [10,12,13]. With this complicated microstructure, it is important to understand the deformation mechanisms of the material so that the alloy can be designed for optimal strength.

This paper focuses on the model AFA alloy Fe–20Cr–30Ni–2Nb–5Al (at. %). Previous studies on the effect of annealing this alloy at 800 °C showed that: Laves Fe_2Nb and B2 NiAl precipitates nucleate in the matrix and grow at longer annealing times; Laves and NiAl precipitates precipitated on the GBs and increased in area coverage with increasing annealing time; and at long annealing times a precipitate free zone (PFZ) formed along the GBs [14,15]. Previous creep studies were performed on this alloy [15,16]. While the previous studies reported the nominal creep temperature as 760 °C, measurement with a thermocouple at the specimen location found that the specimens were actually at 750 °C. These studies found that both the Laves phase and B2 precipitates grew during creep and their volume fraction in the matrix and GB area coverage increased during creep testing [15,16]. A PFZ was also found at long creep times [15,16]. In addition, $L1_2$ -structured Ni_3Al precipitates nucleated in the matrix during the creep tests. These $L1_2$ precipitates then coarsened during creep [15,16]. Prior work has yielded a reasonable understanding of each precipitate's impact on strength at high temperature. Fine Laves precipitates are beneficial to strength, but as they coarsen they are no longer effective strengtheners [15–17]. B2 phase precipitates are soft at high temperatures, and as they coarsen they weaken the material [16,17]. $L1_2$ precipitates are very effective strengtheners, providing most of the high temperature strengthening in these alloys [15,18,19]. GB strengthening through coverage by precipitates in AFA steels and other alloys has also been reported [20,21].

* Corresponding author. 14 Engineering Drive, Hanover, NH 03755, USA.
E-mail addresses: andrew.c.peterson.th@dartmouth.edu (A. Peterson), ian.baker@dartmouth.edu (I. Baker).

https://doi.org/10.1016/j.msea.2021.141219
Received 5 January 2021; Received in revised form 28 March 2021; Accepted 30 March 2021
Available online 8 April 2021

However, the effectiveness of this strengthening mechanism and the actual mechanism are not well understood in AFA alloys. Lastly, a PFZ has been shown to weaken precipitation-hardened alloys [22,23].

In alloys strengthened by second-phase particles, the interactions of dislocations with precipitates are generally grouped into three categories [24–26]. First, dislocations can cut through particles. This process is more likely to occur for particles which are small and/or coherent with the matrix. For soft precipitates, dislocation cutting can occur at larger sizes. Second, the dislocations can by-pass particles by Orowan looping – a process by which the dislocations pass fully around particles and create a loop around the precipitates. The stress necessary for looping to occur is termed the Orowan stress (τ_0). Third, the dislocations can by-pass the particles by climb. Several models of particle by-pass by climb have been proposed. In the Arzt-Ashby model [26] the stress required to overcome a particle is determined by the stress needed to provide the energy to increase the length of the dislocation as it climbs past the particle. The method of climb is dependent on the transition of the dislocation line at the particle surface. In general climb, there is a gradual transition of the dislocation line at the particle surface and the stress needed to overcome the particle is relatively small. In local climb, there is a sharp transition of the dislocation line which requires a much higher stress. However, others have criticized this method of determining the stress needed to climb over the particle because the sharp bends in dislocation lines in local climb would be relaxed by diffusion, resulting in general climb and, thus, much lower values of required stress [27]. Later, Arzt and Wilkinson proposed a creep model where the stress required to climb past a particle is due to the attraction between the dislocation and the particle [28]. In the Arzt-Wilkinson model, when there is little attraction between the particle and dislocation, the required stress is controlled by the stress needed to climb past the particle. When the attraction between the dislocation line and the particle increases, the required stress is controlled by the detachment of the dislocation from the particle. However, with three different precipitates present in the matrix of Fe–20Cr–30Ni–2Nb–5Al at 750 °C, it is not certain which mechanisms will occur and how these mechanisms will change as the size and spacing of the precipitates change.

In addition to precipitation strengthening in the matrix, the coverage of GBs by precipitates could potentially increase the strength via a GB strengthening mechanism. This mechanism has been reported in AFA alloys where it was attributed to reducing GB sliding as result of precipitate coverage [21,29]. Additionally, Zhang et al. developed a model for GB strengthening in dislocation creep, in which the GBs covered by precipitates cause a pile-up of dislocations near the GBs and increase the strength [20]. Based on prior research, it is not yet clear if either of these mechanisms occur in Fe–20Cr–30Ni–2Nb–5Al.

The purpose of this study is to determine which deformation mechanisms are occurring in Fe–20Cr–30Ni–2Nb–5Al at 750 °C. By understanding these mechanisms, AFA alloys can be designed to optimize their strength.

2. Experimental

Fe–20Cr–30Ni–2Nb–5Al (at. %) was cast into 8 kg ingots using split-cast vacuum induction and then press forged into rectangular bars with dimensions 19 mm × 19 mm x 600 mm by Carpenter Technology Corporation. A solutionizing anneal was then performed in an argon atmosphere for 24 h at 1250 °C, resulting in a grain size of ~450 μm. Grain size was calculated by analyzing optical microscopy images using the linear intercept method. Specimens were prepared for both creep tests and high-temperature strain-rate jump tests. The creep specimens were milled into dog-bones with gauge cross-sections dimensions of 2.7 mm × 2 mm and a gauge length of 20 mm. The dog-bones were annealed for 2.4 h at 800 °C in air followed by cooling in air. For high-temperature strain-rate rate jump tests, the alloy was milled into dog-bones with gauge cross-section dimensions of 3 mm × 1.8 mm with a gauge length of 10 mm. The dog-bones were then annealed in air at 760 °C or 800 °C for the various times, followed by an air cooling. The dog-bones for both tests were polished with successively finer silica carbide sandpaper up to 1200 grit, and then further polished with 0.3 μm and 0.05 μm alumina powder to a mirror finish.

Creep tests were performed at 750 °C (as measured at the specimen location) and applied stresses of 35 MPa, 45 MPa, 65 MPa, 75 MPa, and 90 MPa on specimens aged at 800 °C for 2.4 h using home-built, constant-true stress creep jigs, which were based on a design by Garofolo, Richmond, and Domis [30]. The strain was determined from the grip displacement, which was measured using an angular displacement transducer on the creep jig. Creep tests were also performed with dog-bones at 730 °C and 770 °C at 45 MPa in order to determine the activation energy of creep. The 800 °C for 2.4 h heat treatment was chosen because of the good creep resistance observed in preliminary creep testing [16].

High-temperature, strain-rate rate jump tests were performed at 750 °C on dog-bones after annealing at either 800 °C or 760 °C for various times on an Instron model 5969 mechanical testing machine equipped with a vertical furnace. Strain was measured from the grip displacement. The initial strain rate was $5 \times 10^{-5}\ s^{-1}$ engineering strain rate. It was assumed that a steady-state flow stress was reached when the stress stopped increasing, and the strain rate was subsequently increased by order of magnitude steps until it reached $5\times 10^{-2}\ s^{-1}$. All strain rate jump tests proceeded from lowest strain rate to highest strain rate. The order of applied strain rates may introduce some bias to the resulting flow stresses. Three tests were performed at 750 °C for each treatment with the reported flow stress representing the average value. After both creep tests and strain rate jump tests, the load was removed and then the furnace was removed from the sample to allow the dog-bones to air cool. All stresses and strains are reported as true stress and true strain. The applied engineering strain rate is used as an approximation for the true strain rate.

Transmission electron microscope (TEM) samples were prepared by cutting 3 mm diameter cylinders from specimens using an electro-discharge machine. These cylinders were then sliced into thin discs and polished with silica carbide paper to ~100 μm thick. The discs were electro-polished in an electrolyte of 20% nitric acid in methanol at −40 °C to −20 °C, 11 V, ~100 mA, and a flow rate of 15, followed by rinsing alternately in ethanol and methanol three times. Imaging was performed using a FEI Tecnai F20 FEG TEM operated at 200 kV. ImageJ was used to analyze the precipitate size and volume fraction in the images. The size of each precipitate was calculated by manually drawing circles over the $L1_2$ precipitates. To determine the volume fraction, the thickness of the sample was determined using convergent beam electron diffraction according to the method outlined by Williams and Carter [31]. Three images were analyzed for each condition and a 95% confidence interval was used to determine the error.

The electropolished samples for TEM imaging were also mounted in the scanning electron microscope (SEM) to be used for SEM imaging. Imaging was performed on a FEI (Thermo Fisher Scientific) Helios 5CX dual beam field emission gun (FEG) SEM. The backscattered electron (BSE) detector was used to distinguish between precipitates, with the Laves phase precipitates appearing light and the B2 phase precipitates appearing dark [14]. ImageJ was used to perform particle size and volume fraction analysis on the SEM images. The particle analysis tool was used to determine the size of the Laves and B2 particles by setting the threshold to include only light or dark precipitates. The size was calculated as an average equivalent diameter. The volume fraction was also calculated. Particles less than 80 nm in equivalent diameter were not included in the analysis. Three images were analyzed for each condition and a 95% confidence interval was used to calculate the error.

3. Results

3.1. Creep test results

Creep tests were performed on specimens after aging at 800 °C for 2.4 h, which contained very fine Laves phase precipitates in the matrix, as well as Laves and B2 phase precipitates on the GB. This anneal was chosen, because in preliminary creep test results it showed the best creep strength [16].

The creep curves from testing at several stresses at 750 °C are shown in Fig. 1a. This plot clearly shows the increasing creep rate with increasing stress. The creep tests at 75 MPa and 90 MPa were performed until failure. All other creep tests were stopped prior to failure.

Creep tests were performed at 750 °C and 45 MPa for a variety of times in order to analyze the microstructural evolution and dislocation substructure during creep; however, only the longest test is shown in the figure. Fig. 1b shows creep curves at 45 MPa and three different temperatures - 730 °C, 750 °C, and 770 °C – with all of these tests being stopped prior to failure.

3.2. Creep testing microstructure

Prior to creep testing, the alloy consisted of very small Laves phase precipitates, <100 nm average equivalent diameter, in the matrix and Laves phase and B2 precipitates on the GBs with a total GB coverage of 35%, see Fig. 2a. $L1_2$ precipitates were not present prior to creep testing. The microstructure evolved significantly during creep testing. The microstructural evolution of Fe–20Cr–30Ni–2Nb–5Al has been discussed in depth in prior work [15]. Briefly, the Laves phase precipitates in the matrix coarsened and their volume fraction increased; B2 precipitates grew in the matrix and increased in volume fraction; $L1_2$ precipitates nucleated and grew in the matrix and increased in volume fraction; GB coverage by Laves phase and B2 precipitates increased to 80%; and a PFZ formed at long creep times (2000 h and longer). Fig. 2b shows the microstructure of the alloy after creep at 45 MPa and 750 °C for 4000 h. The large Laves phase and B2 matrix precipitates are clearly visible in both the matrix and along the GB, and the inset image shows a BF TEM image of the $L1_2$ matrix precipitates. Note that the microscopy images for Fig. 2 were published in a previous paper [15].

3.3. Dislocation structure during creep

Fig. 3 shows TEM images of the matrix dislocation substructure and microstructure after creep at 45 MPa for different times at 750 °C. Fig. 3a and b shows the microstructure after creep for 250 h where dislocations appear to be primarily gliding through the matrix unimpeded. There is no indication of interaction between the dislocations and either the Laves phase or the B2 precipitates, likely due to the large spacing between these precipitates and the low dislocation density. However, there are signs of some dislocations by-passing the much smaller and more closely-spaced $L1_2$ particles by general climb, see Fig. 3b. Fig. 3c and d shows the microstructure after creep for 1000 h. Again, the dislocations are primarily gliding through the matrix with some general climb observed around the $L1_2$ particles. Little interaction with the larger Laves phase and B2 precipitates occurs. Fig. 3e and f shows the structure after creep for 2000 h. Surprisingly, there is no

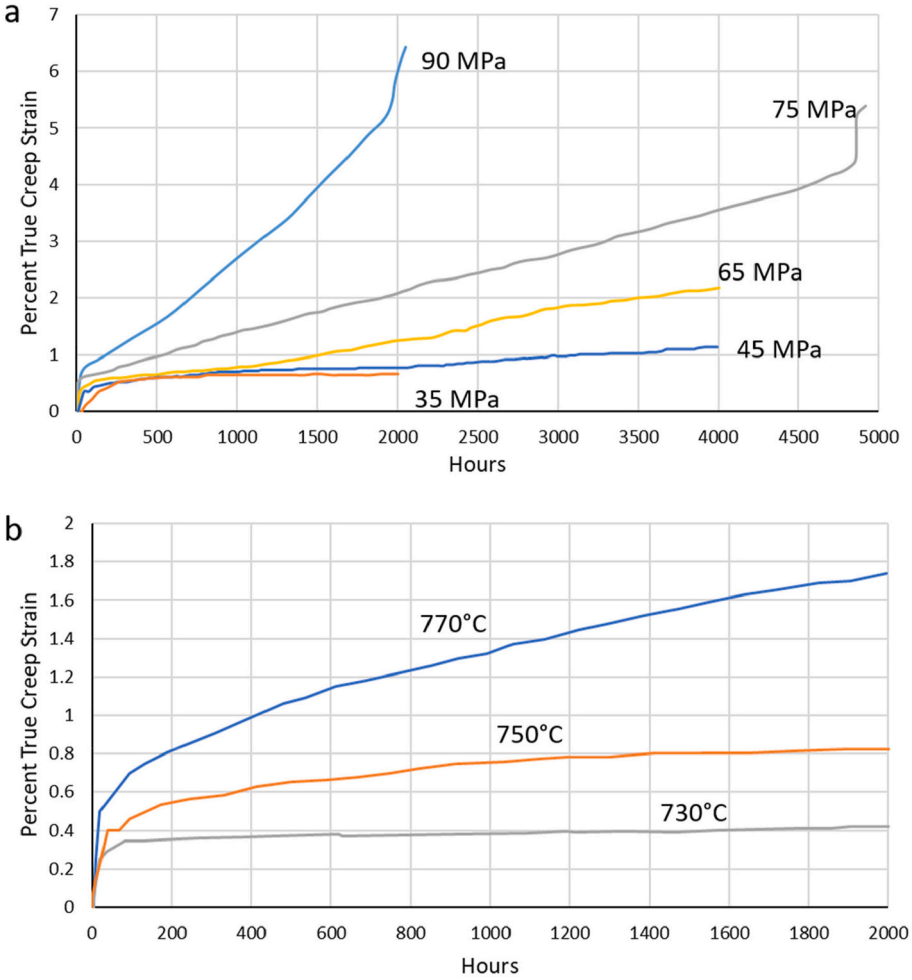

Fig. 1. Creep curves for Fe–20Cr–30Ni–2Nb–5Al at a) 750 °C and various stresses, and b) 45 MPa and various temperatures.

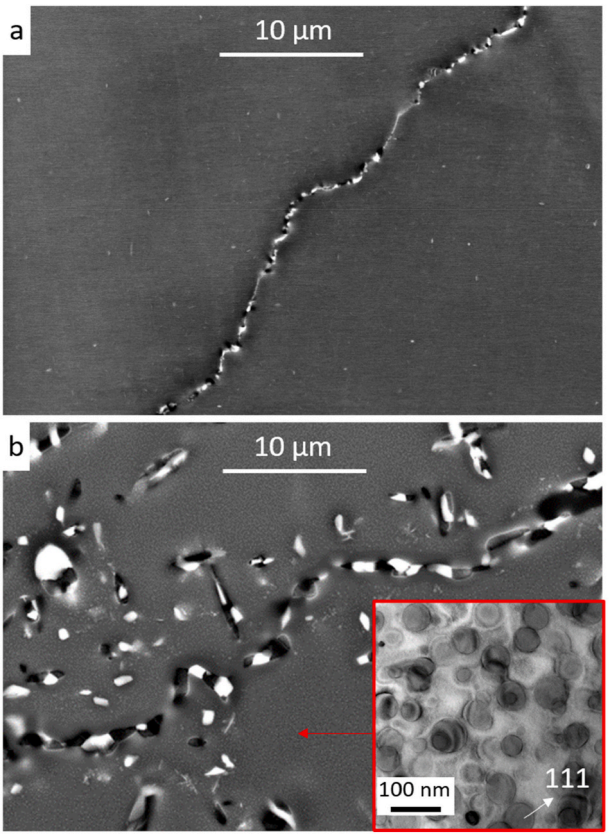

Fig. 2. a) BSE image of the microstructure prior to creep testing, b) BSE image of the microstructure, with bright-field TEM image inset, after creep for 4000 h at 750 °C and 45 MPa.

evidence of dislocations cutting, climbing, or looping past the larger Laves and B2 phase precipitates. However, there does appear to be some dislocation pile-up at the interfaces between these precipitates and the matrix. This would indicate that these large precipitates are acting as barriers to dislocation motion. Fig. 3f clearly shows dislocations climbing past the $L1_2$ precipitates.

In summary, during creep at 45 MPa: the dislocations are initially able to glide through the matrix with only minimal by-pass of the $L1_2$ precipitates needed. As the volume fraction and size of the $L1_2$ precipitates increases with creep time, the dislocations are eventually forced to by-pass these particles by climb. No evidence was found of cutting, looping, or climbing of the Laves and B2 precipitates. However, at long creep times evidence was found of dislocation pile-ups against these much larger precipitates.

Fig. 4 shows TEM images of the dislocation substructure near the GBs. Fig. 4a shows a triple junction after creep at 750 °C and 45 MPa for 4000 h. From this image, it is very clear that there is a large dislocation density near the GBs and the dislocations have begun to pile-up at the GB precipitates. Fig. 4b shows the same triple junction, but a different area. This image shows a dislocation gliding along a slip plane, which then appears to be blocked by a GB precipitate. Fig. 4c is from creep after 1000 h at 750 °C and 45 MPa. With the lower dislocation density, it is more evident that the dislocation density is greater near the GB than it is further away in the matrix. Fig. 4d shows a GB after creep at 730 °C and 45 MPa for 2000 h. At the lower temperature, the GB precipitates have not coarsened as much. However, the dislocation density is still higher near the GB than in the matrix.

3.4. Creep fracture mode

The only creep tests performed until failure were tests at 750 °C and either 75 MPa or 90 MPa. Secondary electron (SE) images of the fracture surface of both crept specimens are shown in Fig. 5. The creep specimens were removed as soon as possible after failure, but there was still some oxidation on the fracture surface. However, intergranular fracture is still clearly evident from the straight lines on the fracture surface, indicating that fracture initiated and then propagated along the GBs.

3.5. Grain boundary sliding

For one creep test, a diamond stylus was used to scribe five lines on each side of the surface of the creep dog-bone specimen that were perpendicular to the direction of the applied stress. The creep test was performed at 750 °C and 90 MPa and terminated after 1500 h. The test was stopped prior to failure to ensure that the markings would not be completely obscured by oxidation. Brief polishing was still needed to reveal the GBs in the SEM. Fig. 6 shows a SE image of a typical diamond stylus marking crossing a GB. No offset was observed at any of the GB/diamond stylus crossings, which suggests that there was no GB sliding or that GB sliding was very minimal.

3.6. Microstructures for strain rate jump tests

For strain rate jump tests, different microstructures were engineered using heat treatments in order to test different features of the microstructure. Because of the test's short duration little microstructural evolution occurs, thus, enabling more variables to be controlled than in creep tests. The tests were performed on the following specimens: 1) annealed at 800 °C for 24 h, and 2) annealed for 4 h at 800 °C, air cooled, and then annealed for 168 h at 760 °C. Going forward, these heat treatments will be referred to as: 800C and 760C, respectively. 800C was selected because in previous testing it showed similar high temperature strength to the 800 °C for 2.4 h anneal, but contained both larger and a higher volume fraction of Laves phase and B2 precipitates in the matrix. This makes it easier to observe the interaction of dislocations with precipitates in the TEM after testing. The 760C anneal was selected through experimentation because it produced similarly sized Laves phase and B2 precipitates in the matrix and on the GB as 800C treatment, but in addition, $L1_2$ precipitates were present in the matrix. Thus, any difference in the high temperature strength of 800C and 760C can be attributed to the $L1_2$ precipitates. Images from the specimens given each treatment are shown in Fig. 7. The treatments are also listed in Tables 1 and 2, which summarize the size and fraction of precipitates in the matrix and on the GBs. During testing, all values for precipitate size and fraction remained within the prior confidence intervals except for the 800C treatment, which did not contain $L1_2$ precipitates prior to testing. In this anneal, very small $L1_2$ precipitates nucleated in the matrix (~13 nm average diameter). TEM images showing this are presented later.

3.7. Strain rate jump test results

High temperature strain rate jump tests were performed at 750 °C with an initial strain rate of 5×10^{-5} s^{-1}, which was then increased by an order of magnitude once a steady-state flow stress was achieved, see Fig. 8. It is obvious that the 760C specimen showed the highest flow stress for each strain rate. However, the 800C specimen shows significantly better ductility than the 760C heat treatment.

3.8. Dislocation structure and fracture mode after strain rate jump tests

Fig. 9 shows four TEM images from the 760C specimen after the strain rate jump test. Fig. 9a shows dislocations by-passing the $L1_2$ precipitates by climb. In this case, it appears to be local climb – where the dislocation has climbed tightly around the precipitate and then bows to the next precipitate with a sharp transition in the dislocation line – while in the creep tests it appeared to be primarily general climb, i.e. the dislocations had more gradual transitions when climbing around the

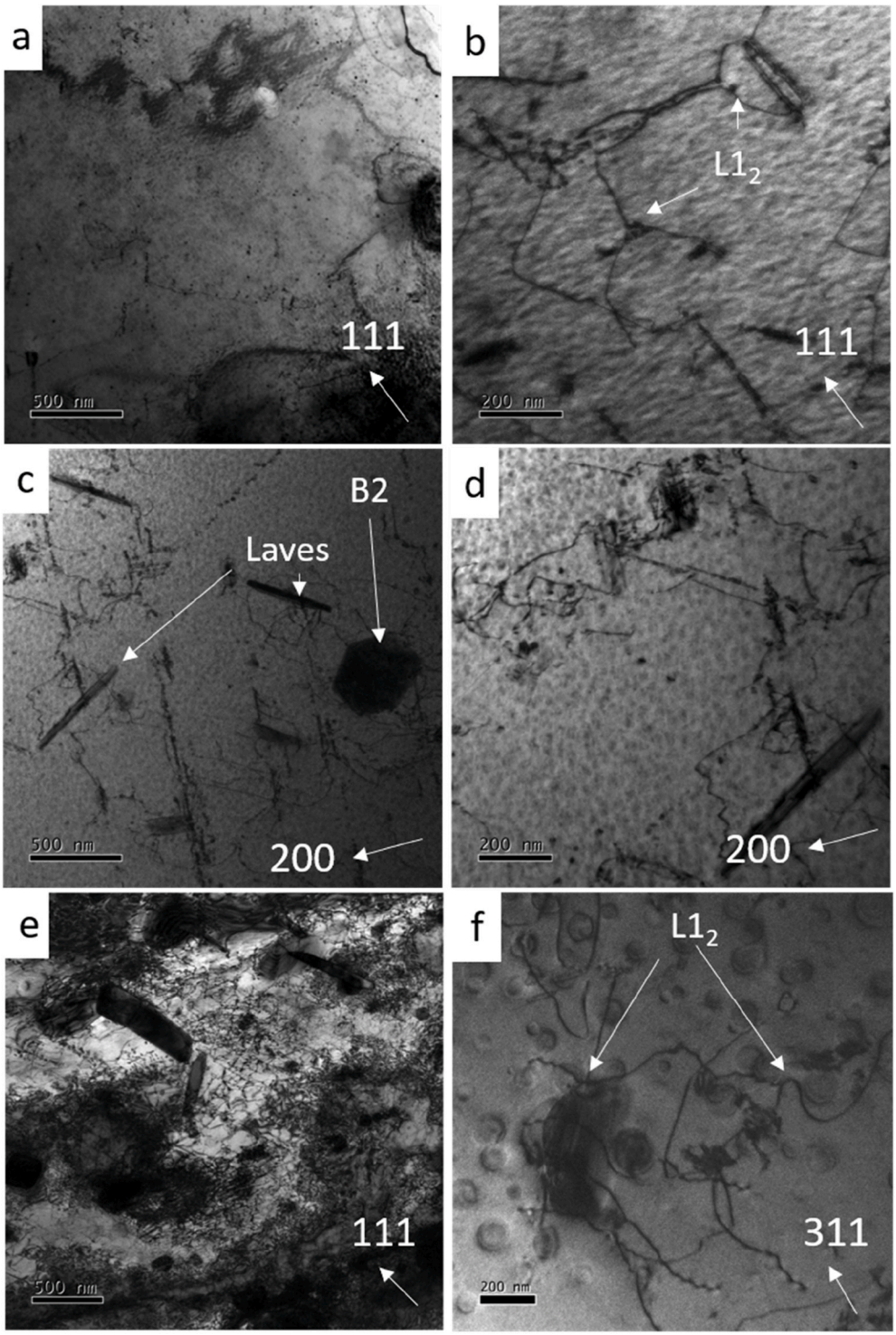

Fig. 3. TEM BF two-beam images of dislocations in Fe–20Cr–30Ni–2Nb–5Al after creep at 750 °C and 45 MPa for a) and b) 250 h, c) and d) 1000 h, and e) and f) 2000 h. Examples of the different precipitates present are arrowed. The operating diffraction vectors are indicated.

precipitates. Fig. 9b is a weak-beam dark-field (WBDF) image showing this same area. Fig. 9c again shows dislocations by-passing $L1_2$ precipitates by climb in the matrix, but also shows a larger build-up of dislocations near the GB. Orowan looping, where the dislocation has looped completely around the precipitate, is present in some instances, but only appears to occur for small precipitates. Dislocation by-pass by climb is clearly the main mechanism for overcoming the precipitates. Fig. 9d shows a Laves phase and B2 precipitate where the dislocations do not appear to by-pass these particles, and instead pile up at the interface. This is similar behavior to what was seen in creep tests.

The 800C treatment showed similar mechanisms for overcoming the precipitates in the matrix as the 760C treatment, despite the fact that there were no $L1_2$ precipitates in the matrix prior to the strain rate jump test. Again, the dislocations did not appear to overcome the larger Laves phase and B2 precipitates via climb or cutting, but instead can be seen climbing past small obstacles in the matrix, see Fig. 10a. Fig. 10b again shows dislocations climbing past small obstacles in the matrix, and also reveals a pile-up of dislocations at the GBs. Fig. 10c and d confirm that

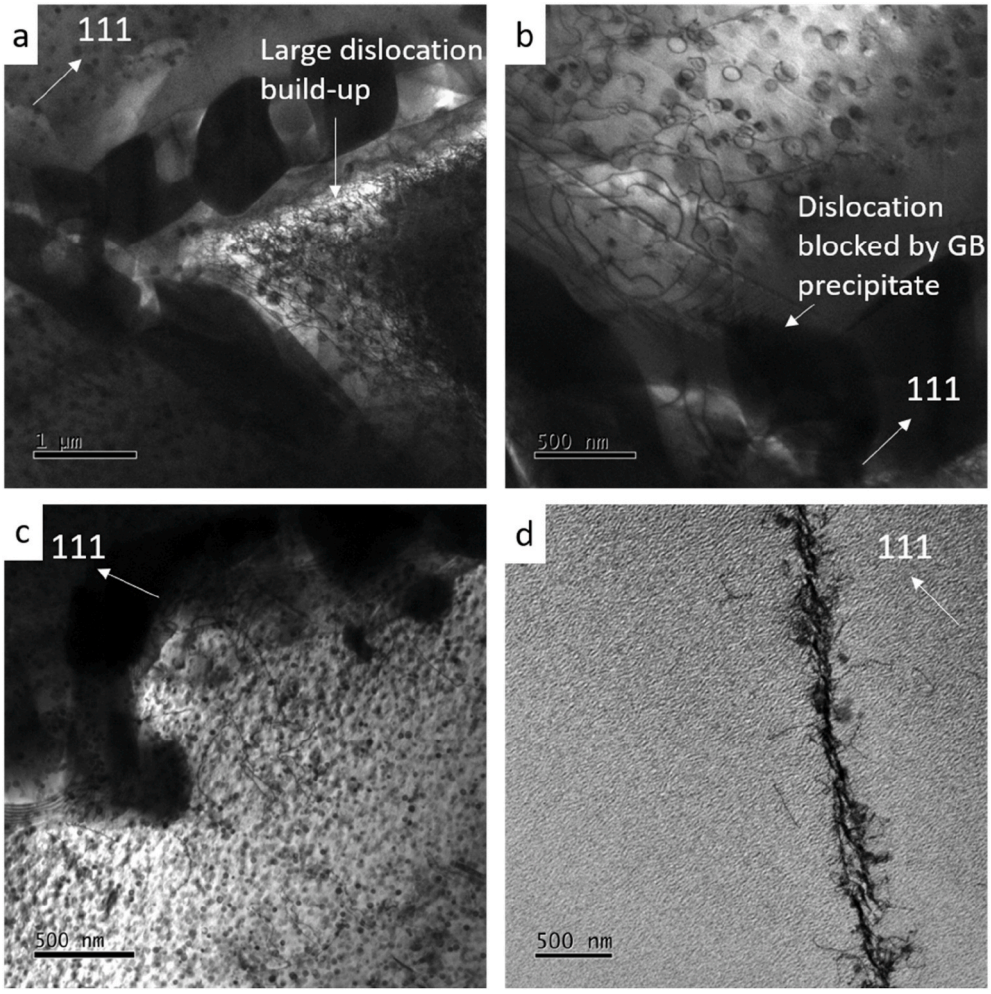

Fig. 4. *Bright-field two-beam TEM images of dislocations near GBs in Fe–20Cr–30Ni–2Nb–5Al after creep at: a) and b) 750°C and* 45 MPa *for 4000 h, c) 750°C and* 45 MPa *for 1000 h, and d) 730°C and* 45 MPa *for 2000 h.* The operating diffraction vectors are indicated.

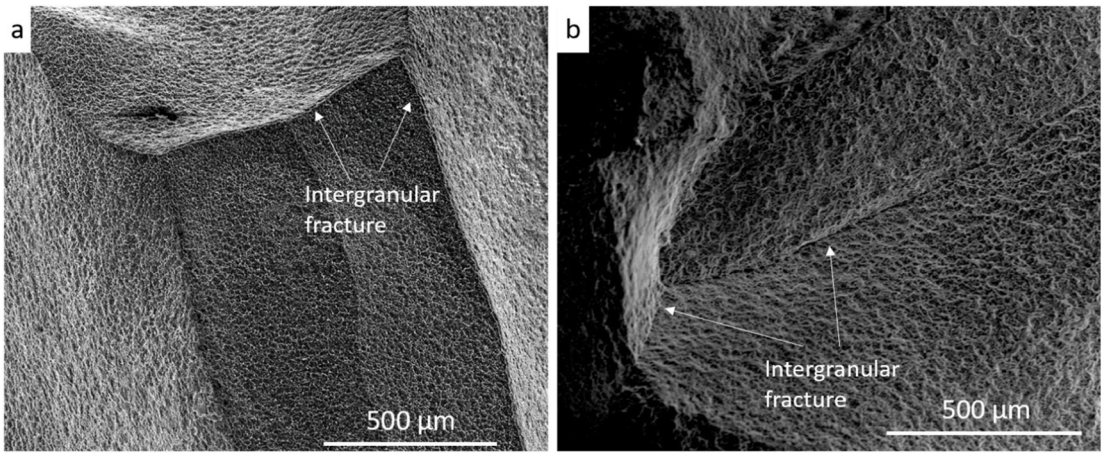

Fig. 5. SE images of the fracture surface of Fe–20Cr–30Ni–2Nb–5Al after creep until failure at a) 750 °C and 75 MPa, and b) 750 °C and 90 MPa.

these small obstacles in the matrix are $L1_2$ precipitates. Fig. 10c shows a high magnification image of one of these small precipitates, and Fig. 10d shows a dark-field image of the same area, with the objective aperture centered around a precipitate diffraction spot. The beam was tilted so that the diffraction spot went down the center of the column. Notice that not all of the very small precipitates appear as light in the dark-field image – this is because there are different orientation relationships between the precipitate and matrix, and not all of them are captured with the chosen diffraction spot. While the 760C treatment showed sharp transitions of the dislocation lines at the precipitates, it is not as clear for the 800C treatment – where the $L1_2$ precipitates are much smaller and further spaced - whether local climb or general climb is occurring.

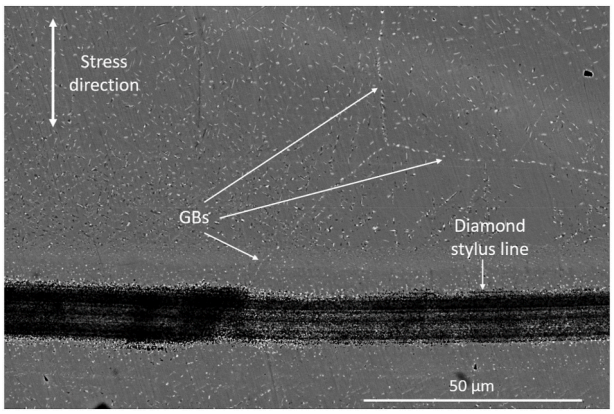

Fig. 6. Diamond stylus marking on Fe–20Cr–30Ni–2Nb–5Al after creep at 750 °C and 90 MPa for 1500 h.

All strain rate jump tests resulted in intergranular fracture, which is the same fracture mode as the creep tests performed until failure in this study, see Fig. 11.

4. Discussion

Fig. 12 is a plot of log strain rate vs log stress for all creep and strain rate jump tests performed at 750 °C. The strain rates of the creep tests were several orders of magnitude slower than those of the strain rate jump tests. Previous research into creep of this alloy indicated that the creep rate changed as the microstructure evolved during creep [15]. To determine the creep rate, the minimum creep rate was determined for each creep test. Each creep test reached a minimum creep rate or near constant creep rate before the end of the test. This plot is useful for determining the creep regime, as the slope of the line, n, is the exponent in the power law creep equation:

$$\dot{\varepsilon} = A\,\sigma^{n}$$

Where $\dot{\varepsilon}$ is the strain rate, σ is the external stress, and A is a constant. An n value of one indicates that diffusion creep is occurring, while an n value of three or greater suggests deformation by dislocation creep.

It is noticeable in Fig. 12 that ñ4 occurs at lower stresses whereas n > 5 occurs at higher stresses. This behavior is commonly reported in a variety of precipitation-hardened alloys, in which there is a 'break' in the value of n within the dislocation creep regime with n ~4 at lower stresses and n > 5 at higher stresses [32]. In this study, the lower values of n correspond to the creep tests performed at 750 °C with stresses ranging from 35 to 90 MPa. With an n value of ~4, creep is likely occurring in the dislocation creep regime. This is supported by the TEM images which showed dislocations gliding and climbing past obstacles in the matrix. This can be further confirmed by determining the activation energy of creep. This can be calculated from:

$$Q = -R\left[\frac{d(ln\dot{\varepsilon})}{d\left(\frac{1}{T}\right)}\right]$$

Where Q is the activation energy for creep, R is the gas constant, and T is the temperature. The activation energy can be determined by plotting the natural log of strain rate versus 1/T for various temperatures and calculating the slope, see Fig. 13. It should be noted that constant σ was used for calculating activation energy as an approximation for constant σ/E. This was done for creep at a stress of 45 MPa and at temperatures of 730 °C, 750 °C, and 770 °C. This small temperature range of tests was used because the $L1_2$ precipitates are near the maximum temperature limit of their stability, as these precipitates are not stable at 800 °C. Even with the small temperature range, the different microstructural evolution at these different temperatures likely has some effect on the calculated activation energy. This yielded a value for the activation energy for creep of 516 kJ/mol. For dislocation creep, it is generally

Table 2
GB precipitate coverage In Fe–20Cr–30Ni–2Nb–5Al after different heat treatments.

Treatment	GB Area Fraction Coverage %		
	Laves	B2	Total
800C	40 ± 6	36 ± 5	76 ± 8
760C	41 ± 5	43 ± 6	84 ± 7

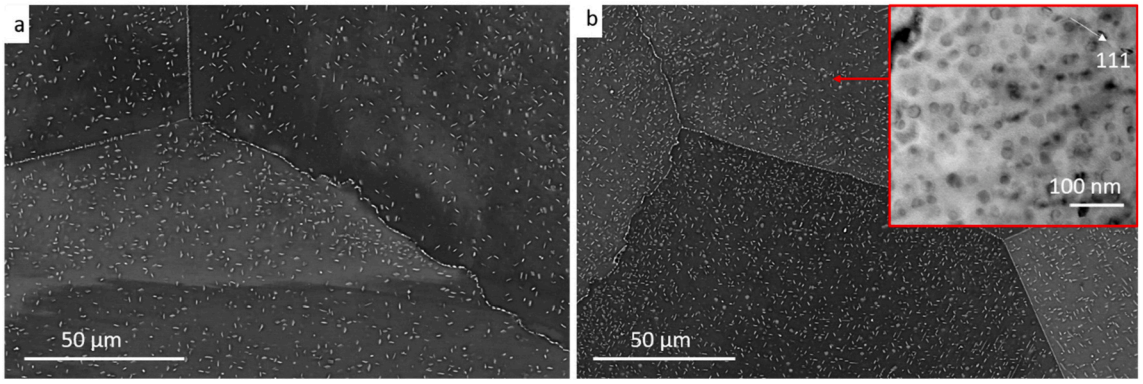

Fig. 7. Images of Fe–20Cr–30Ni–2Nb–5Al after various heat treatments: a) BSE image after treatment 800C and b) BSE image after treatment 760C, with BF TEM image inset showing $L1_2$ precipitates present in the matrix.

Table 1
Precipitate size and volume fraction for Fe–20Cr–30Ni–2Nb–5Al after different heat treatments.

Treatment	Laves		B2		$L1_2$	
	Average Size(nm)	Volume Fraction (%)	Average Size(nm)	Volume Fraction (%)	Average Size(nm)	Volume Fraction (%)
800C	213 ± 21	1.37 ± 0.26	227 ± 33	0.11 ± 0.03	0	0
760C	221 ± 19	1.31 ± 0.35	223 ± 29	0.08 ± 0.03	23 ± 3	0.88 ± 0.13

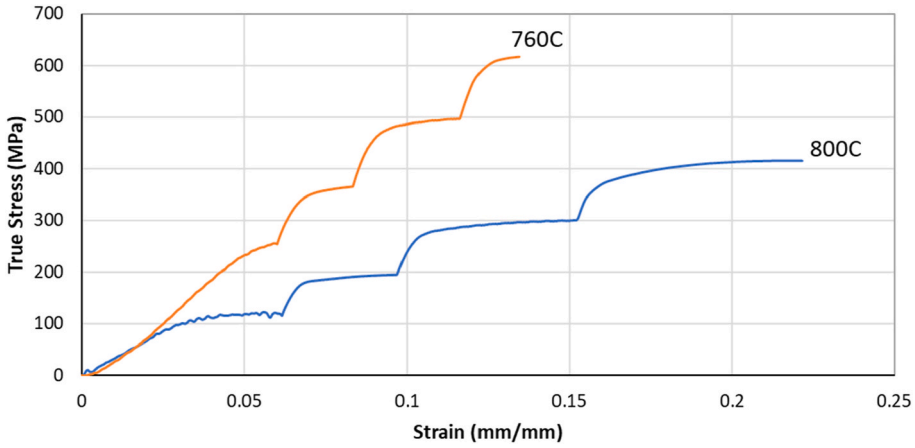

Fig. 8. Strain rate jump tests performed at 750 °C on Fe–20Cr–30Ni–2Nb–5Al after the various heat treatments shown. The initial strain rate was 5×10^{-5} s^{-1} and was increased by an order of magnitude for each 'jump'.

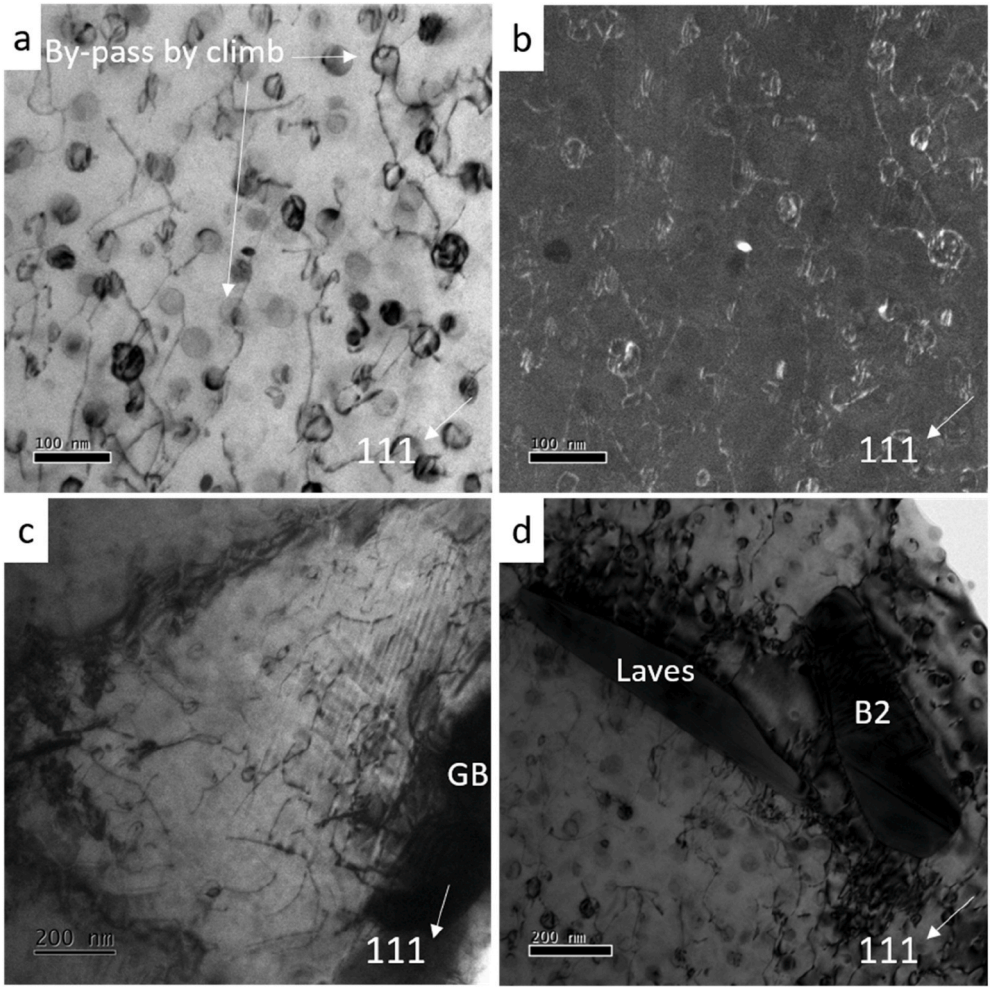

Fig. 9. Dislocation-precipitate interactions in Fe–20Cr–30Ni–2Nb–5Al after strain rate jump tests at 750 °C. a) BF image showing by-pass by climb of $L1_2$ precipitates, b) WBDF image showing the same area as image a) using the g-3g condition c) BF image showing the dislocation build-up near the GB, and d) BF image showing the dislocations have little interaction with the larger Laves and B2 precipitates. The operating diffraction vectors are indicated.

considered that the activation energy for creep is similar to the activation energy for diffusion in the matrix, however, the value calculated here is significantly larger than the activation energy for self-diffusion of Fe in austenite (280 kJ/mol) [33]. However, for many precipitation-hardened alloys it has been reported that activation energy for dislocation creep is significantly higher than that of the activation energy of diffusion, including for a γ′ Ni-base superalloy with activation energy of creep at 546 kJ/mol compared to the activation energy of Ni in Ni of 284 kJ/mol [34]. This shows good agreement with the results here, and further confirms the dislocation creep regime. However, it should be

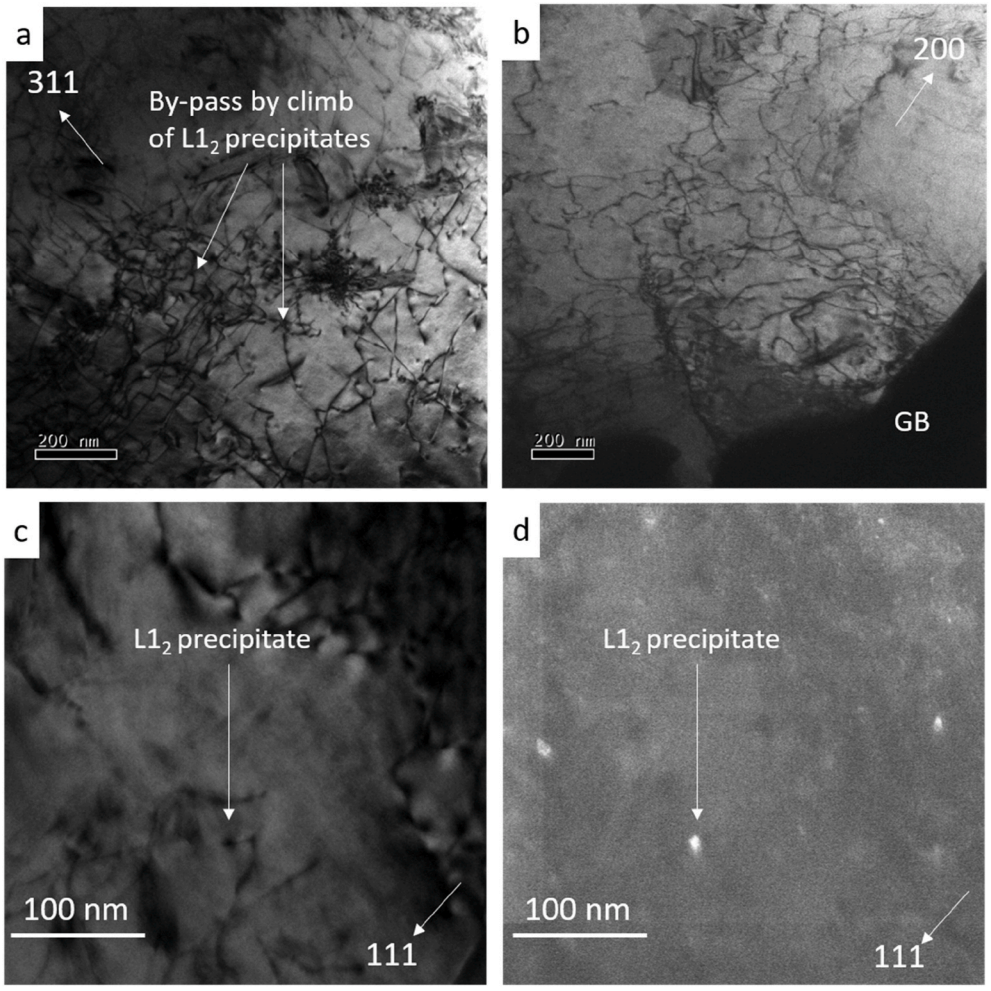

Fig. 10. Dislocation-precipitate interactions in Fe–20Cr–30Ni–2Nb–5Al after annealing at 800 °C followed by strain rate jump tests at 750 °C. a) BF image showing dislocations climbing past small $L1_2$ precipitates in the matrix, b) BF image showing by-pass by climb of the very small $L1_2$ precipitates in the matrix and build-up of dislocations at the GB, c) BF image showing a $L1_2$ precipitate, and d) DF image showing the same precipitate area as (c), with the objective aperture centered around a precipitate diffraction spot. The operating diffraction vectors are indicated.

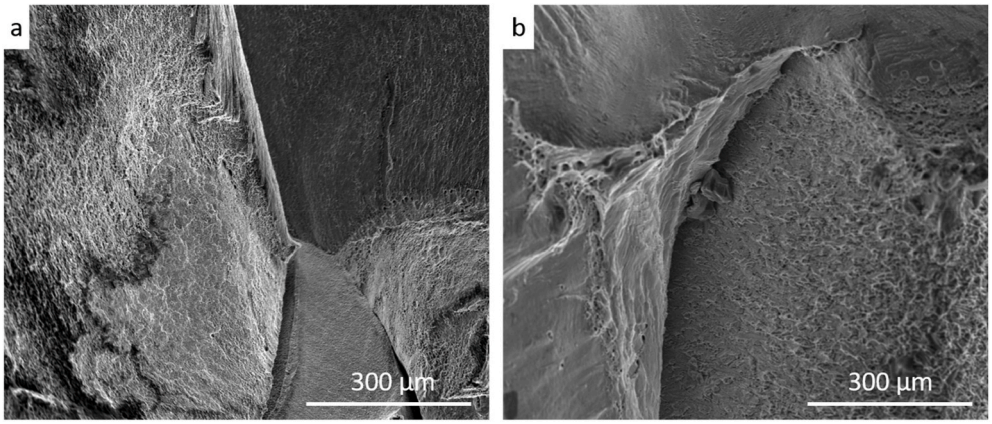

Fig. 11. SE images of fracture surfaces of Fe–20Cr–30Ni–2Nb–5Al after strain rate jump tests to failure at 750 °C: a) Specimen 760C after failure, and b) Specimen 800C after failure.

noted that the activation energy of 516 kJ/mol calculated is quite a bit larger than the value of 282 kJ/mol reported for a different AFA alloy [35].

For the strain rate jump tests, the n values are greater than 5, which is higher than the n value for the creep tests. While n can be calculated for each separate heat treatment, we can also calculate the n value for all heat treatments together. This will give an idea of how well different models explain the effects of precipitate and GB strengthening. When this is done for the power law model, the best fit line has $n = 4.2$ with R^2 of only 0.64, see Fig. 14 which shows the n value for each heat treatment individually as well as a best fit line for all data. Clearly, the power law description is not capturing the true mechanisms of strengthening in this alloy.

For precipitation-hardened materials, it is common to introduce a threshold stress term into the power law creep equation, i.e.

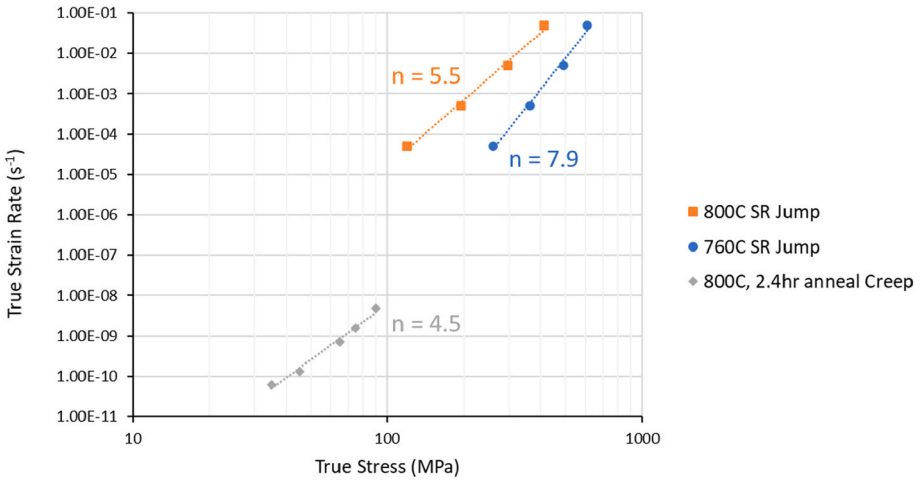

Fig. 12. Log strain rate vs log true stress for both creep tests and strain rate jump tests of Fe–20Cr–30Ni–2Nb–5Al. All tests were performed at 750 °C.

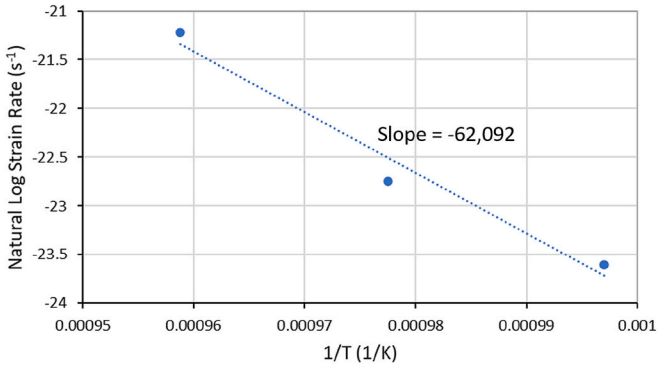

Fig. 13. Natural log strain rate versus reciprocal temperature for creep tests of Fe–20Cr–30Ni–2Nb–5Al at 45 MPa.

$$\dot{\varepsilon} = B(\sigma - \sigma_{th})^n$$

Where σ_{th} is the threshold stress, which represents the stress needed for the dislocations to overcome the particles in the matrix, and B is a constant. The threshold stress depends on which mechanism the dislocations use to by-pass the particles: cutting, Orowan looping, or climb. TEM imaging was performed after creep testing and strain rate jump tests in order to determine which mechanism occurred. As discussed in the Results section, by-pass by climb is the main mechanism by which the dislocations overcome precipitates in the matrix during strain rate jump tests, and this mechanism is only occurring with the $L1_2$ precipitates. Several methods have been proposed to calculate the threshold stress when dislocations by-pass precipitates by climb. Both methods rely on the Orowan stress, which can be calculated from:

$$\tau_0 = \frac{Gb}{L - 2r}$$

Where τ_0 is the Orowan stress (the stress needed to operate the Orowan looping mechanism), G is the shear modulus, b is the Burgers vector, L is the mean interparticle spacing, and r is the mean particle radius. G is approximately 50 GPa and b is approximately 0.253 nm for AFA alloys [35,36]. L and r can be calculated from the average particle size and volume fraction. For the Arzt-Ashby model, several estimates have been made of the threshold stress required to by-pass particles by climb. This term can be approximated as $\sim 0.3\tau_0$ to $\sim 0.45\tau_0$ for local climb and by $\sim 0.05\tau_0$ to $\sim 0.1\tau_0$ for general climb [24,26,37]. For this paper, $0.4\tau_0$ will be used for local climb and $0.075\tau_0$ will be used for general climb.

The threshold stress term due to climb in the Arzt-Wilkinson model can be calculated as $0.4\,k^{5/2}\tau_0$, where k is the relaxation parameter (i.e. with no attraction $k = 1$, with maximum attraction $k = 0$). It should be noted that when $k = 1$, this equation is quite similar to the Arzt-Ashby equation for local climb. In addition to this threshold stress term due to climb, there is also a threshold stress term for the dislocation to detach from the particle. This detachment threshold stress term dominates except when there is less than 6% attraction between the dislocation and the particle [28,34]. The detachment threshold stress term is $\tau_0\sqrt{1-k^2}$. The benefit of this theory is that the attractive interaction between the dislocation and particle explains why local climb can be stable. However, the value of k cannot be predicted theoretically and must be approximated with creep data using the methodology outlined by Rösler and Arzt [25]. The value of k was determined for each condition which

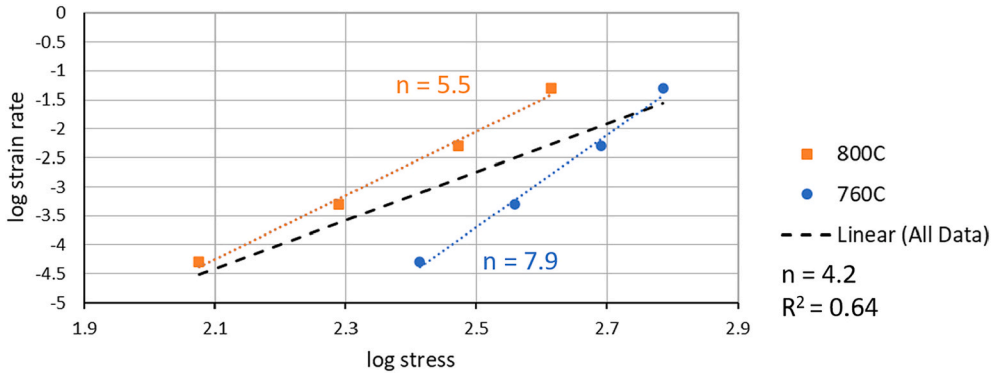

Fig. 14. Log_{10} true strain rate versus log_{10} true stress for the strain rate jump tests of Fe–20Cr–30Ni–2Nb–5Al at 750 °C.

was tested in strain rate jump test using the activation energy calculated during creep tests. The value of k was calculated to be 0.92 and 0.86 for the treatments 760C and 800C, respectively. These values of k are very similar to the value of 0.93 obtained for a γ' strengthened Ni-base superalloy [25,38]. As the k values are less than 0.94, the threshold stress term is controlled by the detachment stress and not the climb. However, it should be noted that since k is very close to 0.94, the threshold stress due to local climb and threshold stress due to detachment are approximately the same for the Arzt-Wilkinson model.

After determining the correct model to use, the stress needed to by-pass the particles by climb would then be inserted as σ_{th} in the power law creep equation by taking twice the calculated shear threshold stress to obtain the tensile threshold stress. For each treatment, the threshold stress is calculated for each model using measurements taken after testing, see Table 3.

To determine the most appropriate model of threshold stress, it is common to plot $\dot{\varepsilon}^{1/n}$ versus stress to graphically determine the value of threshold stress, see Fig. 15. This requires an assumption of the value of n. As noted before, n is commonly reported as 5 for AFAs and similar alloys [35,36], and this value will be used here. This plot yields the following values for graphical threshold stress: 154 MPa for 760C and 32 MPa for 800C. For the 760C treatment, this graphically determined value is closest to the theoretical threshold stress values predicted by local climb using the Arzt-Ashby model and due to the detachment stress after local climb using the Arzt-Wilkinson model. As both theoretical values of threshold stress are the same, this graphically determined value does not help determine which model is better. For the 800C treatment, the graphically determined value is similarly closest to the threshold stress values predicted by local climb using the Arzt-Ashby model and due to the detachment stress after local climb using the Arzt-Wilkinson model. For consistency, and because the Arzt-Wilkinson model has the benefit of explaining why local climb is stable, the Arzt-Wilkinson model of using the threshold stress due to detachment will be used.

This model can now be plotted as log strain rate vs log effective stress ($\sigma - \sigma_{th}$) as shown in Fig. 16. This plot shows that the strengthening arising from dislocations having to by-pass $L1_2$ precipitates by climb fits the data well. The slopes of the lines, n, are approximately 4.5 and 5.4. The expected value of n for dislocation climb in an austenite matrix is approximately 5, as reported in research into similar AFA alloys [35,36]. The linear fit of all data shows an n value of 4.3 with an R^2 value of 0.85, which represents a much better fit than the power law equation without the threshold stress. These results suggest that using a threshold stress term to model the strengthening effect of $L1_2$ precipitates works well to explain the significant strengthening seen with presence of $L1_2$ precipitates in the matrix. However, there are a couple questions left unanswered: 1). The graphically determined threshold stress value for the 760C treatment is much higher than any theoretical value for climb past the $L1_2$ precipitates. What is the source of the additional threshold stress? 2). Using the threshold stress term calculated with the detachment stress for the 800C treatment results in an n value of much less than 5. Is general climb a better model for the smaller and further spaced $L1_2$ precipitates in this treatment?

It is possible that the GB precipitates are providing additional strengthening to the alloy. Previously, a GB strengthening effect has been reported in AFA alloys that was attributed to the precipitates covering the GBs and thereby reducing GB sliding [21,29]. The creep test with a diamond stylus lines showed that there was no, or limited, GB sliding, which is consistent with this idea. However, the strain rates used in the strain rate jump test are likely too fast for GB sliding to occur. Thus, these tests are not testing for the effects of GB sliding.

Zhang et al. [20] developed a model to describe GB strengthening in the dislocation climb regime. In this model, the GBs covered by precipitates present an obstacle to dislocation movement. Thus, a pile-up of dislocations occurs at the GBs, creating a difference in local stresses at the GB versus the matrix. By matching the strains near the GB and in the matrix, a term for the GB obstacle stress was developed, which can then be used in a similar way to the particle threshold stress in the power law creep equation, i.e.

$$\dot{\varepsilon} = C(\sigma - \sigma_{th} - \sigma_{BO})^n$$

Where C is a constant and σ_{BO} is the obstacle stress for the GB, and can be calculated from:

$$\sigma_{BO} = (m)(2KGb/d)^{\frac{1}{2}}(\sigma)^{\frac{1}{2}}\left(1 - \frac{\sigma_{th}}{\sigma}\right)$$

Where m is the GB fraction coverage, K is a constant that is usually about 23, and d is grain size.

The experimental observations are consistent with this theory of GB strengthening occurring, as the TEM imaging of specimens after both creep tests and strain rate jump tests showed a very high density of dislocations near the GBs. As such, it would be reasonable to apply the Zhang model of GB strengthening to this alloy. Several iterations were performed to find the best matrix precipitate threshold stress using this model. For the 760C treatment, the model showed best fit using $\sigma_{th} =$ 118 MPa as calculated from either the local climb model or detachment stress after local climb model. For the 800C treatment, the model showed best fit using $\sigma_{th} = 5$ MPa as calculated using the general climb model. Both are reasonable assumptions based on the presented micrographs showing precipitate-dislocation interactions. The GB coverage by precipitates after strain rate jump tests was calculated as 78% for 760C and 77% for 800C. Table 4 shows σ, σ_{th}, and σ_{BO} for each strain rate for each heat treatment. These data are plotted as log strain rate versus log effective stress, where the effective stress is now $\sigma - \sigma_{th} - \sigma_{BO}$, in Fig. 17.

This plot also shows a good linear fit for each heat treatment, with n values of 5.2 and 5.3. Additionally, a linear fit of all data points shows an n value of 5.0 with an R^2 value of 0.93. This R^2 value represents an improvement over the model which only used a threshold stress for the matrix $L1_2$ precipitates and the n values closely match the predicted value of n. Additionally, the model is consistent with the presented TEM images for each treatment.

Due to the significant microstructural evolution during creep, it is difficult to fit the creep test data at different stresses to these models. However, in a previous paper we showed that the creep rate evolved with the microstructure and this could be modeled well using the Zhang model for GB strengthening [15].

While the GBs appear to be strengthening the alloy both by blocking dislocation motion and limiting GB sliding, all tests still failed via intergranular fracture. This suggests that the GBs are still the weak spot in the microstructure – even in the strain rate jump tests, where a PFZ had not yet formed. This suggests that the coarsened Laves phase and B2 precipitates along the GB are ultimately the weakest point in the microstructure. It is likely that the PFZ that forms at long creep times further decreases the strength near the GBs.

An interesting feature of the strain rate jump test stress-strain curves is the 'waviness' in the curves at low strain rates (5×10^{-5} s^{-1}) for the

Table 3
$L1_2$ precipitate properties and corresponding threshold stress values for Fe–20Cr–30Ni–2Nb–5Al after strain rate jump tests at 750 °C.

Treatment	Diameter (nm)	L (nm)	τ_0 (MPa)	Local σ_{th} (MPa)	General σ_{th} (MPa)	Detachment σ_{th} (MPa)
760C	27	111	148	118	22	118
800C	13	367	36	29	5	36

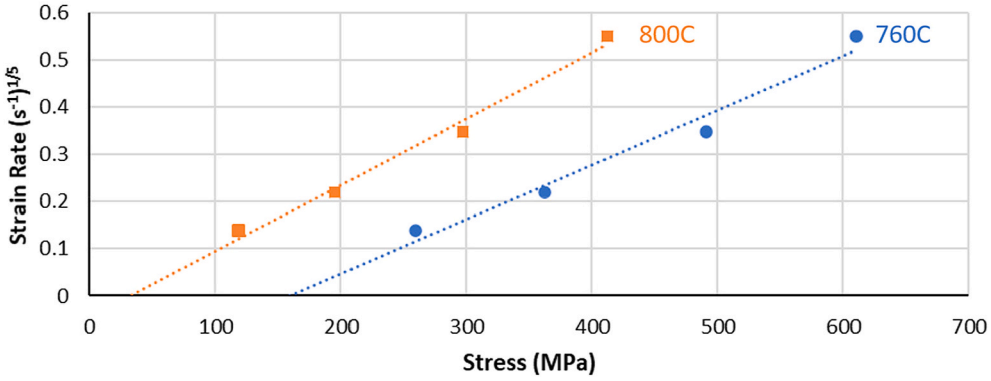

Fig. 15. Strain rate to the power of (1/5) versus true stress for Fe–20Cr–30Ni–2Nb–5Al after strain rate jump tests at 750 °C for various treatments.

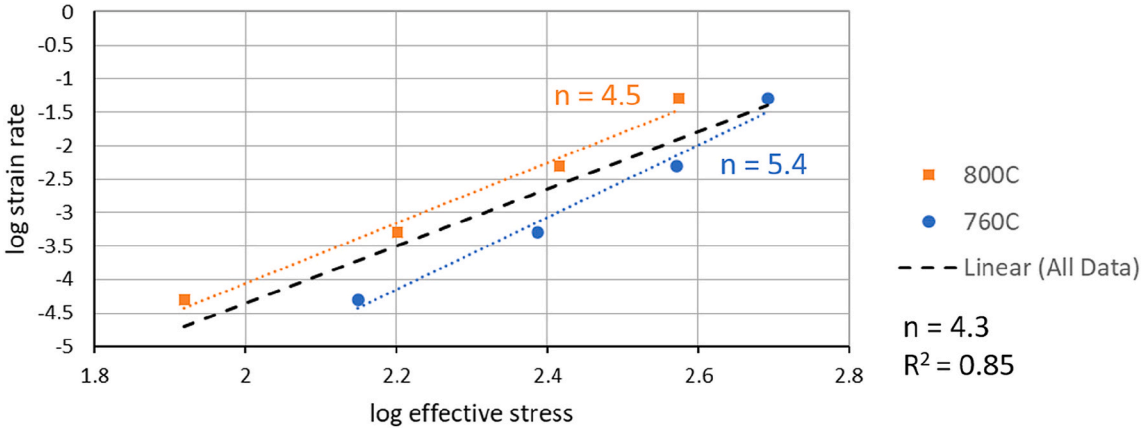

Fig. 16. Log_{10} strain rate versus log_{10} effective true stress for Fe–20Cr–30Ni–2Nb–5Al for strain rate jump tests at 750 °C using a threshold stress term for climb past $L1_2$ precipitates.

Table 4
Flow stress (σ), threshold stress (σ_{th}), and obstacle stress (σ_{BO}) for strain rate jump tests at 750°C on Fe–20Cr–30Ni–2Nb–5Al for various heat treatments.

Applied Strain Rate (s^{-1})	760C			800C		
	σ (MPa)	σ_{th} (MPa)	σ_{BO} (MPa)	σ (MPa)	σ_{th} (MPa)	σ_{BO} (MPa)
0.00005	259	118	8	119	5	9
0.0005	362	118	11	195	5	12
0.005	491	118	15	297	5	15
0.05	610	118	18	412	5	18

800C treatment – see Fig. 18. While these serrations could be indicative of dynamic strain aging, the serrations which indicate dynamic strain aging are generally much higher frequency. The serrations observed here occur much less often, so we suggest that these serrations are when dislocations become blocked by an obstacle in the matrix before overcoming it. This would explain why the serrations are much more apparent in the 800C treatment than in the 760C treatment. In the 800C treatment, the $L1_2$ precipitates are much further spaced. As a result, the dislocations could move freely through the matrix before being halted by a precipitate. In the 760C treatment, the dislocations would need to continuously climb past the closely-spaced $L1_2$ precipitates. The serrations are only apparent for the lowest strain rate. There are two possible reasons for this. First, as the strain rate increases the dislocations will be moving much quicker through the matrix and more continuously encountering obstacles. Second, $L1_2$ precipitates nucleate in the matrix during testing and as a result they will become more closely spaced with increased time.

5. Conclusions

The effects of different microstructures in Fe–20Cr–30Ni–2Nb–5Al at 750 °C on the high-temperature deformation behavior have been studied by performing both creep tests and strain rate jump tests on specimens given various heat treatments. A combination of SEM and TEM imaging was used to characterize the microstructure during testing, and TEM imaging was also used to examine dislocation/particle interactions. The experimental data was fitted to models describing the deformation mechanisms. This work led to following conclusions:

1. Creep at 750 °C and stresses of 35–90 MPa is occurring by dislocation creep. TEM imaging reveals that dislocations are gliding through the matrix and by-passing $L1_2$ precipitates by general climb. The number of these climbing interactions increases as the dislocation density and volume fraction of $L1_2$ precipitates increase with creep time.
2. Strain rate jump tests at 750 °C clearly show that the $L1_2$ precipitates provide substantial strengthening to the alloy. This can be modeled well by dislocation climb around these precipitates.
3. There is no evidence of dislocations overcoming the Laves and B2 precipitates via a cutting, looping, or climbing mechanism during creep or strain rate jump tests at 750 °C. This is likely due to the large spacing between these particles. The $L1_2$ precipitates become the dominant strengthening precipitate in the matrix due to the small interparticle spacing. However, at higher strain levels there is dislocation pile up at the larger Laves and B2 precipitates which could have some strengthening effect.
4. It is important to note that none of the models used in this work considered the matrix Laves phase and B2 precipitates. Previous

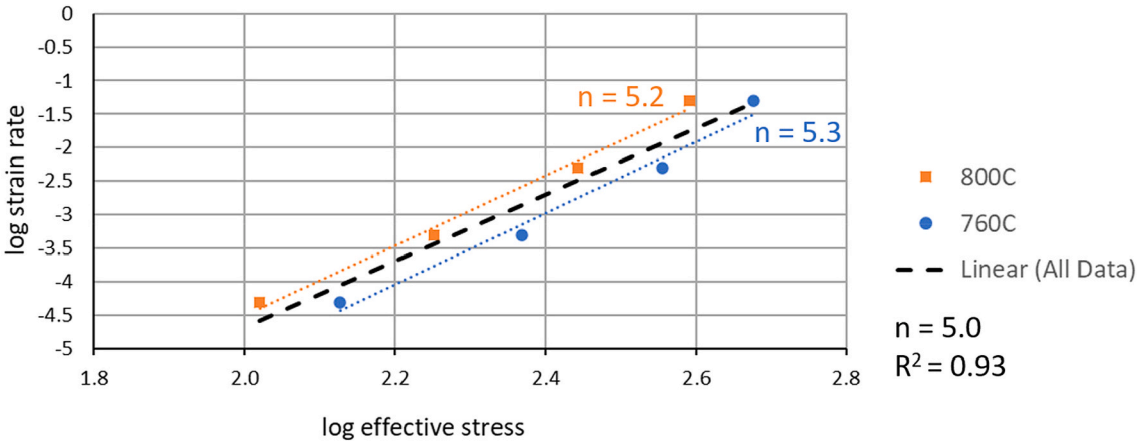

Fig. 17. Log_{10} strain rate versus log_{10} effective true stress for Fe–20Cr–30Ni–2Nb–5Al for strain rate jump tests at 750 °C using both a threshold stress term and a GB obstacle stress term.

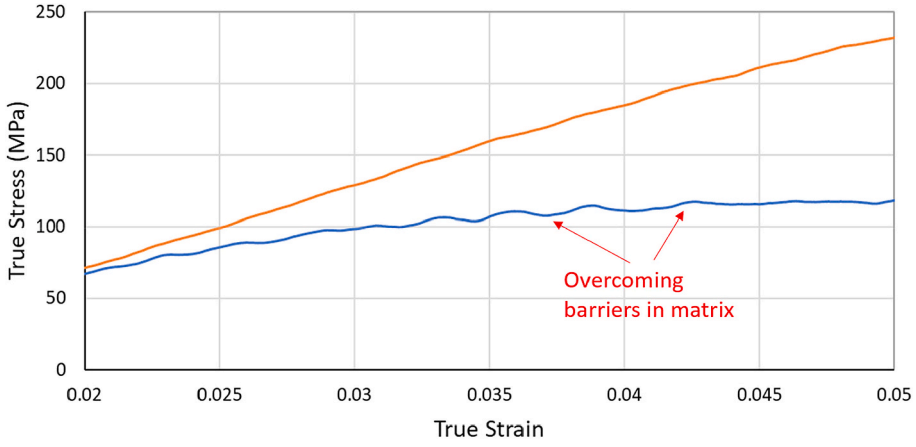

Fig. 18. Stress-strain curves for strain rate jump tests for Fe–20Cr–30Ni–2Nb–5Al at 750 °C, showing the section of the curve for the 5×10^{-5} s^{-1} strain rate.

research on this alloy showed a significant decrease in high temperature strength as these precipitates increased in size [16].

5. Creep tests showed no evidence of GB sliding. It is likely that GB coverage by precipitates either prevents or greatly reduces GB sliding.
6. The GB precipitates likely act as a barrier to dislocation movement. The presented data fits this model very well and is supported by TEM imaging.
7. All tests ultimately failed along the GBs. This indicates that the large Laves phase and B2 precipitates along the GBs are ultimately the weak point in the microstructure.

Data availability

The raw/processed data required to reproduce these findings cannot be shared at this time as the data also forms part of an ongoing study.

CRediT authorship contribution statement

Andrew Peterson: Conceptualization, Methodology, Investigation, Writing – original draft, Visualization, Formal analysis. **Ian Baker:** Conceptualization, Resources, Writing – review & editing, Funding acquisition.

Declaration of competing interest

The authors declare that they have no known competing financial interests or personal relationships that could have appeared to influence the work reported in this paper.

Acknowledgements

This research was supported by National Science Foundation Grant DMR 1708091. Any opinions, findings, and conclusions or recommendations expressed in this material are those of the author(s) and do not necessarily reflect the views of the NSF. Michael Schmidt of Carpenter Technology Corporation (Wyomissing, PA) provided the ingots. The use of the Dartmouth Electron Microscope Facility is gratefully acknowledged.

References

[1] R. Viswanathan, J.F. Henry, J. Tanzosh, G. Stanko, J. Shingledecker, B. Vitalis, R. Purgert, U.S. Program on materials Technology for ultra-supercritical coal power plants, J. Mater. Eng. Perform. 14 (2005) 281–292, https://doi.org/10.1361/10599490524039.

[2] J.P. Shingledecker, I.G. Wright, Evaluation of the materials Technology required for a 760?C power steam boiler. https://www.osti.gov/biblio/931631, 2006 accessed June 26, 2019.

[3] M. Takeyama, Novel concept of austenitic heat resistant steels strengthened by intermetallics, Mater. Sci. Forum 539–543 (2007) 3012–3017. https://doi.org/10.4028/www.scientific.net/MSF.539-543.3012.

[4] M.P. Brady, Y. Yamamoto, M.L. Santella, P.J. Maziasz, B.A. Pint, C.T. Liu, Z.P. Lu, H. Bei, The development of alumina-forming austenitic stainless steels for high-temperature structural use, J. Occup. Med. 60 (2008) 12–18, https://doi.org/10.1007/s11837-008-0083-2.
[5] M.P. Brady, Y. Yamamoto, M.L. Santella, B.A. Pint, Effects of minor alloy additions and oxidation temperature on protective alumina scale formation in creep-resistant austenitic stainless steels, Scripta Mater. 57 (2007) 1117–1120, https://doi.org/10.1016/J.SCRIPTAMAT.2007.08.032.
[6] B.A. Pint, J.P. Shingledecker, M.P. Brady, P.J. Maziasz, Alumina-forming austenitic alloys for advanced recuperators, in: Turbo Expo 2007, vol. 3, ASME, 2007, pp. 995–1002, https://doi.org/10.1115/GT2007-27916.
[7] Y. Yamamoto, M.P. Brady, Z.P. Lu, P.J. Maziasz, C.T. Liu, B.A. Pint, K.L. More, H. M. Meyer, E.A. Payzant, Creep-resistant, Al2O3-forming austenitic stainless steels, Science 316 (2007) 433–436, https://doi.org/10.1126/science.1137711.
[8] P. Kofstad, Defects and transport properties of metal oxides, Oxid. Metals 44 (1995) 3–27, https://doi.org/10.1007/BF01046721.
[9] U. Heubner, Nickel Alloys, Marcel Dekker, 1998. https://books.google.com/books/about/Nickel_Alloys.html?id=-ufvbPfm3BUC. (Accessed 29 June 2019).
[10] Y. Yamamoto, M. Takeyama, Z.P. Lu, C.T. Liu, N.D. Evans, P.J. Maziasz, M. P. Brady, Alloying effects on creep and oxidation resistance of austenitic stainless steel alloys employing intermetallic precipitates, Intermetallics 16 (2008) 453–462, https://doi.org/10.1016/J.INTERMET.2007.12.005.
[11] Y. Yamamoto, M.P. Brady, Z.P. Lu, C.T. Liu, M. Takeyama, P.J. Maziasz, B.A. Pint, Alumina-forming austenitic stainless steels strengthened by Laves phase and MC carbide precipitates, Metall. Mater. Trans. 38 (2007) 2737–2746, https://doi.org/10.1007/s11661-007-9319-y.
[12] M.P. Brady, J. Magee, Y. Yamamoto, D. Helmick, L. Wang, Co-optimization of wrought alumina-forming austenitic stainless steel composition ranges for high-temperature creep and oxidation/corrosion resistance, Mater. Sci. Eng. 590 (2014) 101–115, https://doi.org/10.1016/J.MSEA.2013.10.014.
[13] Y. Yamamoto, M.P. Brady, M.L. Santella, H. Bei, P.J. Maziasz, B.A. Pint, Overview of strategies for high-temperature creep and oxidation resistance of alumina-forming austenitic stainless steels, Metall. Mater. Trans. 42 (2011) 922–931, https://doi.org/10.1007/s11661-010-0295-2.
[14] G. Trotter, I. Baker, The effect of aging on the microstructure and mechanical behavior of the alumina-forming austenitic stainless steel Fe–20Cr–30Ni–2Nb–5Al, Mater. Sci. Eng. 627 (2015) 270–276, https://doi.org/10.1016/j.msea.2014.12.072.
[15] A. Peterson, I. Baker, Microstructural evolution of Fe-20Cr-30Ni-2Nb-5Al AFA Steel during creep at 760°C, Mater. Sci. Eng., A (2020) 140602, https://doi.org/10.1016/j.msea.2020.140602.
[16] I. Baker, N. Afonina, Z. Wang, M. Wu, Preliminary creep testing of the alumina-forming austenitic stainless steel Fe-20Cr-30Ni-2Nb-5Al, Mater. Sci. Eng. 718 (2018) 492–498, https://doi.org/10.1016/J.MSEA.2018.01.090.
[17] Y. Yamamoto, M.L. Santella, M.P. Brady, H. Bei, P.J. Maziasz, Effect of alloying additions on phase equilibria and creep resistance of alumina-forming austenitic stainless steels, Metall. Mater. Trans. 40 (2009) 1868–1880, https://doi.org/10.1007/s11661-009-9886-1.
[18] B. Hu, G. Trotter, Z. Wang, S. Chen, Z. Cai, I. Baker, Effect of boron and carbon addition on microstructure and mechanical properties of the aged gamma-prime strengthened alumina-forming austenitic alloys, Intermetallics (2017), https://doi.org/10.1016/j.intermet.2017.06.011.
[19] Y. Yamamoto, G. Muralidharan, M.P. Brady, Development of L12-ordered Ni3(Al, Ti)-strengthened alumina-forming austenitic stainless steel alloys, Scripta Mater. 69 (2013) 816–819, https://doi.org/10.1016/J.SCRIPTAMAT.2013.09.005.
[20] J.S. Zhang, P.E. Li, W.X. Chen, J.Z. Jin, Grain boundary precipitation strengthening in high temperature creep of Fe15Cr25Ni alloys, Scripta Metall. 23 (1989) 547–551, https://doi.org/10.1016/0036-9748(89)90449-3.
[21] I. Tarigan, K. Kurata, N. Takata, T. Matsuo, M. Takeyama, Novel concept of creep strengthening mechanism using grain boundary Fe $_2$ Nb Laves phase in austenitic heat resistant steel, MRS Proc 1295 (2011), https://doi.org/10.1557/opl.2011.558 mrsf10-1295-n06-03.
[22] T. Krol, D. Baither, E. Nembach, Quantification of the detrimental effects of precipitate free zones on the yield strength of a superalloy, Scripta Mater. 48 (2003) 1189–1194, https://doi.org/10.1016/S1359-6462(02)00566-3.
[23] D. Baither, T. Krol, E. Nembach, *In-situ* transmission electron microscopy study of dislocation processes at precipitate-free zones in a γ' -strengthened superalloy, Philos. Mag. A 83 (2003) 4011–4029, https://doi.org/10.1080/14786430310001603445.
[24] J. Zhang, Creep of second phase particles strengthened materials, in: High Temp. Deform. Fract. Mater., Elsevier, 2010, pp. 83–101, https://doi.org/10.1533/9780857090805.1.83.
[25] J. Rösler, E. Arzt, A new model-based creep equation for dispersion strengthened materials, Acta Metall. Mater. 38 (1990) 671–683, https://doi.org/10.1016/0956-7151(90)90223-4.
[26] E. Arzt, M.F. Ashby, Threshold stresses in materials containing dispersed particles, Scripta Metall. 16 (1982) 1285–1290, https://doi.org/10.1016/0036-9748(82)90484-7.
[27] R. Lagneborg, Bypassing of dislocations past particles by a climb mechanism, Scripta Metall. 7 (1973) 605–613, https://doi.org/10.1016/0036-9748(73)90222-6.
[28] E. Arzt, D.S. Wilkinson, Threshold stresses for dislocation climb over hard particles: the effect of an attractive interaction, Acta Metall. 34 (1986) 1893–1898, https://doi.org/10.1016/0001-6160(86)90247-6.
[29] S.W. Chen, C. Zhang, Z.X. Xia, H. Ishikawa, Z.G. Yang, Precipitation behavior of Fe2Nb Laves phase on grain boundaries in austenitic heat resistant steels, Mater. Sci. Eng. 616 (2014) 183–188, https://doi.org/10.1016/J.MSEA.2014.07.104.
[30] F. Garofalo, O. Richmond, W.F. Domis, Design of apparatus for constant-stress or constant-load creep tests, J. Fluids Eng. Trans. ASME. 84 (1962) 287–293, https://doi.org/10.1115/1.3657303.
[31] D.B. Williams, C.B. Carter, Transmission Electron Microscopy: A Textbook for Materials Science, Springer US, 2009, https://doi.org/10.1007/978-0-387-76501-3.
[32] R. Lagneborg, B. Bergman, The Stress/creep Rate Behaviour of Precipitation-Hardened Alloys, 2014, https://doi.org/10.1179/030634576790431462.
[33] M.F. Ashby, H.J. Frost, Deformation-mechanism Maps, Oxford Pergamon Press, 1982.
[34] J. Rösler, E. Arzt, The kinetics of dislocation climb over hard particles-I. Climb without attractive particle-dislocation interaction, Acta Metall. 36 (1988) 1043–1051, https://doi.org/10.1016/0001-6160(88)90158-7.
[35] D.Q. Zhou, X.Q. Xu, H.H. Mao, Y.F. Yan, T.G. Nieh, Z.P. Lu, Plastic flow behaviour in an alumina-forming austenitic stainless steel at elevated temperatures, Mater. Sci. Eng. 594 (2014) 246–252, https://doi.org/10.1016/j.msea.2013.11.021.
[36] B. Hu, I. Baker, The effect of thermo-mechanical treatment on the high temperature tensile behavior of an alumina-forming austenitic steel, Mater. Sci. Eng., A (2016), https://doi.org/10.1016/j.msea.2015.11.036.
[37] R.S.W. Shewfelt, L.M. Brown, High-temperature strength of dispersion-hardened single crystals II, Theory, Philos. Mag. 35 (1977) 945–962, https://doi.org/10.1080/14786437708232636.
[38] E. Arzt, J.H. Schroeder, HIGH TEMPERATURE STRENGTH OF ODS SUPERALLOYS DUE TO DISPERSOID-DISLOCATION INTERACTION, 1986.